PVDF-Based Microfabricated Tactile Sensor for Minimally Invasive Surgery

Mohammad Ameen Qasaimeh*, Saeed Sokhanvar, Javad Dargahi, and Mojtaba Kahrizi, *Member, IEEE*

Abstract—**This paper aimed to develop a miniaturized tactile sensor capable of measuring force and force position in minimally invasive surgery. The *in situ* measurement of tactile information is a step forward toward restoring the loss of the sense of touch that has occurred due to shift from traditional to minimally invasive surgeries. The sensor was designed such that it can sense low forces which could be comparable to those produced by pulsating delicate arteries, yet can withstand high forces comparable to grasping forces. The influence of some hidden anatomical features, such as lumps, voids, and arteries, on the stress distribution at the grasping surface was studied. In this paper, the capability of the sensor to determine and locate any point load was also investigated. The proposed sensor was designed and manufactured to be highly sensitive, using polyvinylidene fluoride (PVDF). The microfabrication procedure of the sensor, including corner compensation for toothlike projections and patterning of PVDF film, was discussed. The micromachined sensor was tested, and the experimental results were compared with the results of 3-D finite element modeling.** [2007-0286]

Index Terms—**Microelectromechanical devices, minimally invasive surgery (MIS), piezoelectric polyvinylidene fluoride (PVDF), tactile sensor.**

I. INTRODUCTION

TWO decades ago, a special surgical procedure called minimally invasive surgery (MIS) using specialized tools was introduced [1]. In the beginning, MIS applications were limited to specific kinds of operations, such as thoracic surgery [2]. Nowadays, MIS has become a standard surgical procedure and is often used in place of traditional open surgery. MIS has been widely accepted and recommended because of its benefits over the traditional open surgeries. In many open surgeries, the damage caused to skin, muscle, connective tissue, and bone in order to reach the region of interest can outweigh the benefits of the therapeutic procedure itself. MIS reduces the suffering caused by conventional surgical procedures by reducing the incision size [3], [4]. These smaller incisions result in numerous benefits, including less pain during the recovery period, reduced blood loss and scarring, faster recovery time, shorter hospitalization, fewer complications due to infection, and better cosmetic results. Overall, MIS provides better treatment at reduced costs [1].

While there are many advantages of MIS, the procedure, as it is currently being practiced, has drawbacks, including the lack of tactile feedback, reduced location perception and dexterity due to restricted vision, difficulty in handling the instruments, and very restricted mobility [5]. During most of the surgeries, the tissues under operation are very soft and sensitive to any excessive force. They are also hidden and located at awkward locations that make the surgery more difficult and sensitive. In such situations, a serious challenge faces the surgeon, and improved tactile sensing of tissue properties is required [5], [6]. To perform MIS more effectively, the surgeon needs to be able to feel the grasping forces, sense the pressure of blood vessels and ducts during the procedure, and detect any embedded lumps inside the grasped organs [7]–[12]. This ability is of great use during manipulation tasks such as grasping internal organs and suturing and removing tissues [13].

As MIS is intrinsically a precise procedure, the associated staff, tools, and sensors need to be precise and accurate with high sensitivity [6]. The required precision of the associated tactile sensing lies in the range of a few micrometers to millimeters [8]. In addition, the typical tactile sensors which are recommended for use during MIS operations have to be small in size and highly sensitive, as well as have low manufacturing and integration costs [3], [6], [8]. The microelectromechanical systems (MEMS) technology could be used in the MIS tactile sensing field in order to manufacture very small microtactile sensors which can be custom made to the surgeon's requirements [8]. These microfabricated tactile sensors are creating a revolution in the field of minimally invasive endoscopic surgery [8], [14], [15]. Additionally, considering that these sensors can be manufactured and produced in large batches, the resulting low unit cost also allows for their disposability [8], [14], [16], which obviates the necessity of cleaning, thereby cutting costs and providing safer surgeries [4], [5].

II. RELATED WORK

Dargahi *et al.* [17] report on the design and microfabrication of a robust piezoelectric endoscopic toothlike tactile

*M. A. Qasaimeh is with the Tactile Sensing and Medical Robotics Laboratory, Department of Mechanical and Industrial Engineering, and also with the MEMS and NanoDevices Laboratory, Department of Electrical and Computer Engineering, Concordia University, Montréal, QC H3G 1M8, Canada (e-mail: mohammad.qasaimeh@mail.mcgill.ca).

S. Sokhanvar and J. Dargahi is with the Tactile Sensing and Medical Robotics Laboratory, Department of Mechanical and Industrial Engineering, Concordia University, Montréal, QC H3G 1M8, Canada (e-mail: sokhan@mit.edu; dargahi@encs.concordia.ca).

M. Kahrizi is with the MEMS and NanoDevices Laboratory, Department of Electrical and Computer Engineering, Concordia University, Montréal, QC H3G 1M8, Canada (e-mail: mojtaba@ece.concordia.ca).

sensor with good linearity and high dynamic response. The sensor, however, was unable to adequately indicate the presence of blood vessels and embedded lumps. In another study, a polyvinylidene fluoride (PVDF)-based tactile sensor for MIS application was presented, and the sensor proved to be capable of recognizing the grasping forces [18], [19]. Nevertheless, given the fact that it has several parts that are difficult to align and assemble, it cannot be considered as a good candidate for batch manufacturing and commercial use. In addition, the sensor failed to properly detect low-magnitude forces, such as blood vessel pulses. Moreover, the sensor is active only on the teeth regions, as the other regions are inactive.

Another tactile sensor for use in MIS was recently presented by Sokhanvar *et al.* [20]. Their PVDF-based sensor was able to detect applied force and position. However, the difficulty of aligning and assembling the sensor is a major obstacle in batch manufacturing and commercial use. Moreover, the sensor is active only on the teeth, and the other regions are inactive areas and cannot detect any tactile properties.

The design and analysis of a membrane-based tactile sensor for MIS applications were also presented by Golpaygani *et al.* [15]. The designed sensor is active only on the mesa points (flat-topped projections), and hence, no tactile information can be gained from the other areas. In addition, the proposed sensor is not toothlike and, hence, not suitable for grasping soft slippery tissues. Metha [21] proposed a capacitive micromachined endoscopic toothlike pressure sensor. Although it is able to measure a few grams of the applied force, it is unable to estimate embedded lumps. A silicon tactile imager based on an array of capacitive cells was developed by Suzuki *et al.* [22]. In another work, a piezoresistive pressure sensor which could be catheter mounted was presented [23]. The capacitive mechanism has also been used in tactile sensing [24]. In addition, on-chip signal processing associated with a silicon pressure sensor was introduced [25]. However, all of these sensors have a thin diaphragm and are not generally designed to carry loads and recognize the grasping forces in the MIS graspers, which can be high in many applications.

This paper presents a new tactile sensor for MIS applications, which has low manufacturing costs, a level of biocompatibility, and the ability to integrate with the existing commercial endoscopic graspers. The proposed prototype is microfabricated using PVDF piezoelectric film as the sensing elements. Largely used for measuring low dynamic forces, PVDF is an ideal sensing material because of its responsiveness to a wide range of frequencies, relatively high mechanical strength, and high sensitivity [16].

Until now, to the best knowledge of the authors, there has not been comprehensive work on the precise measurement of forces involved in blood vessel pulses. Although some researchers [10], [26], [27] have reported these forces to be in the range of several grams to few tens of grams, precise measurements are still required. The reason perhaps is due to lack of sensitive tactile sensors with the capabilities that are required for these experiments. In addition, pulsation varies from one vessel to another and depends on the vessel size,
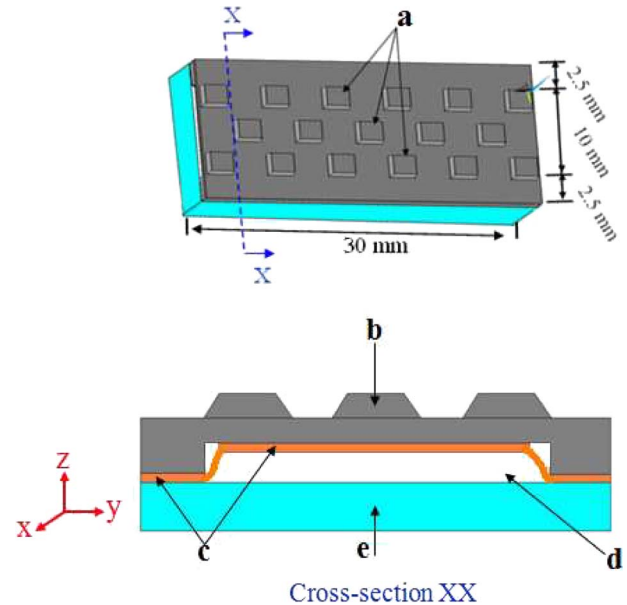

Fig. 1. Proposed sensor structure. (a) Teeth shapes. (b) Micromachined silicon layer (first layer). (c) PVDF layer at the supports and middle (second layer)—see Figs. 7 and 11 for more details. (d) U channel (gap for deflection). (e) Plexiglas layer (third layer).

depth inside the tissue, and the blood pressure. In this paper, based on the limited available data, we accepted few grams of force for a typical pulsating artery and designed the sensor for that.

In this paper, it is shown that the proposed sensor is able to estimate grasping forces, to locate point loads, and, also, to sense small loads. Locating point loads potentially is useful in the detection of embedded lumps, and the capability of sensing small loads could be used in the detection of the pulsating blood vessels inside grasped tissue.

The sensor is toothlike along the length and width directions, and therefore is suitable for grasping, handling, twisting, and lifting soft slippery tissues. Although the proposed sensor is specifically designed for use in MIS, it can easily be altered to be used in any robotic and teleoperations in which tactile information is required.

III. SENSOR DESIGN

As shown in Fig. 1, the proposed sensor is composed of three layers. The top layer is a silicon plate micromachined from a silicon wafer. The second or middle layer is composed of the sensing elements and is fabricated from PVDF film. Finally, the upper two layers are supported by a third layer of Plexiglas. These three layers would form one jaw of a grasper. If both jaws of the grasper are equipped with the sensors, more tactile information can be collected [28]. In this paper, however, only one jaw is considered to be equipped with the sensor, and the other jaw is a regular jaw (dummy), which only applies compressive force to the grasped object. It is important here to mention that the jaw with the sensor surface and the other dummy jaw are designed to be interdigitated with each other (off-tooth for the sensor surface associates with on-tooth on the dummy, and vice versa), which probably has a better stress

distribution across the tissue and causes less damage to the tissue.

Silicon was chosen for this application as it is simple to fabricate in batches using MEMS technology and also due to its satisfactory mechanical properties. In addition, the required electronics, such as charge amplifiers and conditioning circuits, can be built on the same wafer, using silicon-based MEMS technology. PVDF is a known piezoelectric material in the tactile sensing field. It is inexpensive compared with other piezoelectric materials, is biocompatible, and is well matched with MEMS technology as it can be integrated with microdevices using different methods.

The first layer was microfabricated to form the required teeth shapes on top and to form a deformable plate in the middle. The designed teeth on top are required for firm grasping of soft tissues. The middle plate is designed to be deformed under grasping action. The supports, on the other hand, hold the silicon plate and provide a suitable gap which is necessary for the plate deflection. The silicon layer is 30 mm in length, with a width of 15 mm, and the supports' width is 2.5 mm on each side. Micromachined out of a 500-μm-thick wafer, the thickness of the top plate is 100 μm, and the height of the supports is 200 μm, leaving a gap of the same height for deflections. The teeth are the frustum of square-based pyramids with a height of 200 μm. The top surface of the pyramid is a 2×2 mm square. The other dimensions of the pyramids are restricted by the two latter dimensions and the specifications of the silicon planes. In the microfabricated silicon layer, the inclined (111) planes form sidewalls of the pyramids with an angle of 54.74° with the xy plane.

The second layer of the sensor was microfabricated from PVDF film to perform as the sensing elements of the sensor. A 25-μm-thick double-sided metalized and prepoled piezoelectric PVDF film was used in microfabrication. The middle part of the PVDF film, working in the extensional mode, was glued to the internal face of the top plate. When, due to a compressive load, the silicon plate deflects, the glued PVDF would also be stretched, and a voltage signal would be registered. Both ends of the PVDF film, working in the thickness mode, are sandwiched between the supports of the silicon plate and the supporting Plexiglas layer. In case of any compression pressure on the silicon layer, these PVDF films at the supports are compressed, and a voltage signal would be created. The middle PVDF part was 30 and 10 mm in length and width, respectively. Each PVDF part at the supports was 30 and 2.5 mm in length and width, respectively. At the microfabrication stage, a total of nine sensing elements arranged in three columns was patterned on a single PVDF film. Each column, referred to as a sensing unit, was composed of three sensing elements, with two at the supports (pairs) and one in the middle (see Figs. 7 and 11). To electrically separate the nine sensing elements, one side of the metalized PVDF was patterned, forming nine metalized islands. The other metalized side was used as a common (bottom) electrode. The third layer, which acts as a base, could be of any rigid material, including silicon. However, since there was no necessity of using silicon, a Plexiglas layer was instead used. The dimensions of the base were 30, 15, and 2 mm for length, width, and thickness, respectively. Plexiglas was used

to support the first two layers of the sensor and to be the connection layer with the commercial endoscope tool while assembling.

IV. SENSOR MODELING

In order to evaluate the performance of the proposed sensor, it was modeled and analyzed using ANSYS version 10, a commercial finite element analysis software. This model was used to determine the deformation of the sensor and the output voltage at the PVDF sensing elements for different loading conditions. The toothlike shape of the etched silicon layer was also studied.

A. Finite-Element Model

The silicon and Plexiglas layers were modeled using SOLID45 element which is used for the 3-D modeling of solid structures. It is defined by eight nodes having three degrees of freedom at each node—translations in the nodal x-, y-, and z-directions. The SOLID227, a 3-D coupled-field element, was used for the modeling of the piezoelectric PVDF layer. It has strong capabilities when dealing with problems pertinent to piezoelectricity. The SOLID227 element has ten nodes, with up to five degrees of freedom per node, and supports elastic large deflections [29]. The Strong (simultaneous, full) coupling method, where the general matrix equation is given by the following form, was used [30]:

$$\begin{bmatrix} [K_{11}] & [K_{12}] \\ [K_{21}] & [K_{22}] \end{bmatrix} \begin{Bmatrix} \{X_1\} \\ \{X_2\} \end{Bmatrix} = \begin{Bmatrix} \{F_1\} \\ \{F_2\} \end{Bmatrix} \tag{1}$$

where $[K]$ is the structural stiffness matrix, $\{X\}$ is the displacement vector, and $\{F\}$ is the force vector. The coupled effect is accounted for by the presence of the off-diagonal submatrices $[K_{12}]$ and $[K_{21}]$.

The matrix equation for the SOLID227 element as a piezoelectric element is given by the following [30]:

$$\begin{bmatrix} [M] & [0] \\ [0] & [0] \end{bmatrix} \begin{Bmatrix} \{\ddot{u}\} \\ \{\ddot{V}\} \end{Bmatrix} + \begin{bmatrix} [C] & [0] \\ [0] & [0] \end{bmatrix} \begin{Bmatrix} \{\dot{u}\} \\ \{\dot{V}\} \end{Bmatrix}$$
$$+ \begin{bmatrix} [K] & [K^Z] \\ [K^Z]^T & [K^d] \end{bmatrix} \begin{Bmatrix} \{u\} \\ \{V\} \end{Bmatrix} = \begin{Bmatrix} \{F\} \\ \{L\} \end{Bmatrix} \tag{2}$$

where

$$\{F\} = \{F^{\text{nd}}\} + \{F^{\text{th}}\} + \{F^{\text{ac}}\} + \{F^{\text{pr}}\}$$
$$\{L\} = \{L^{\text{nd}}\} + \{L^C\} + \{L^{\text{SC}}\}$$

where $[M]$, $[C]$, and $[K]$ are the structural mass, the structural damping, and the structural stiffness matrices, respectively. The matrices $[K^Z]$ and $[K^d]$ represent the piezoelectric stiffness and the dielectric coefficient matrices, respectively. The vectors $\{F^{\text{nd}}\}$, $\{F^{\text{th}}\}$, $\{F^{\text{ac}}\}$, and $\{F^{\text{pr}}\}$ are the applied nodal force, the thermal strain force, the force vector due to acceleration effects, and the pressure load vector, in that order. The charge vectors $\{L^{\text{nd}}\}$, $\{L^C\}$, and $\{L^{\text{SC}}\}$ indicate the applied nodal charge, the charge density load vector, and the surface charge density load vector, correspondingly.
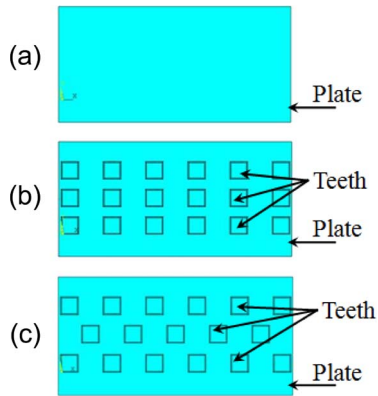
Fig. 2. Different teeth configurations on the microfabricated silicon layer were analyzed and compared. (a) Simple plate of 100-μm thickness. (b) Plate of 100-μm thickness with teeth on top, distributed on a matrix configuration. (c) Plate of 100-μm thickness with teeth on the top, distributed with a checked pattern.

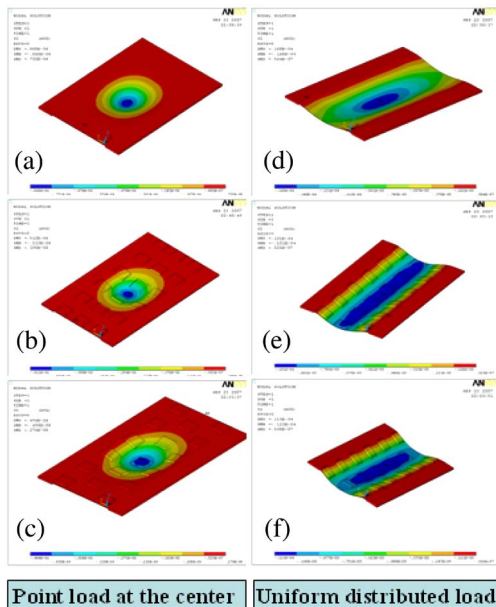Point load at the center   Uniform distributed load

Fig. 3. Deformed states of the studied configurations for (a), (b), and (c) point load and (d), (e), and (f) distributed load.

B. Finite Element Analysis to Determine Best Teeth Configuration

In order to investigate the influence of different configurations of toothlike shapes etched on silicon layer, three cases were simulated and examined for the largest deflection and, hence, higher voltage output. These included a simple plate of 100-μm thickness, a matrix arrangement of the teeth on a 100-μm-thick plate, and a check pattern of the teeth, again, on a 100-μm-thick plate. Fig. 2 shows the three configurations.

For each configuration, two sets of simulations were carried out. Fig. 3(a)–(c) shows the deformation profiles as a result of applying a point load at the center of the plates, namely, the simple, matrix, and check configurations, respectively. Alternatively, Fig. 3(d)–(f) shows the deflection profile of each configuration when a distributed load is applied.

The deformation profiles of silicon layer for all three configurations, when a point load was applied, are compared and
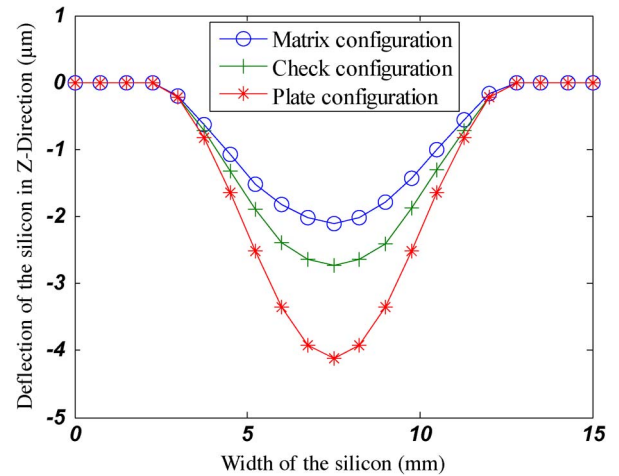

Fig. 4. Deflection profiles of three configurations while a point load is applied at the center of the plates.
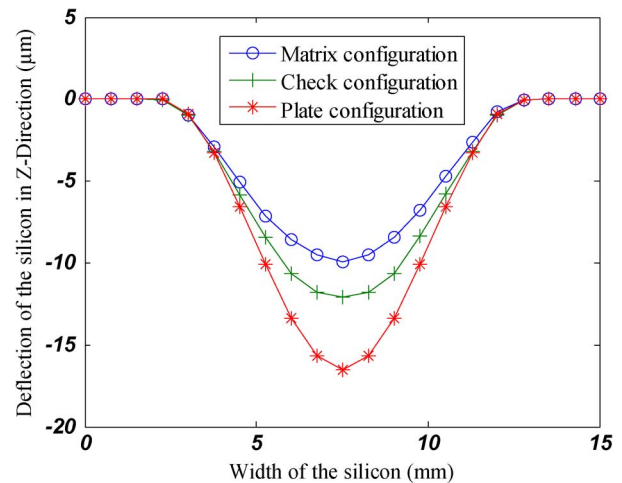

Fig. 5. Profiles of three configurations while a distributed load is applied at the center of the plates.

shown in Fig. 4. The deformation in Fig. 4 is in the z-direction and along the thickness of the plate. Alternatively, Fig. 5 shows the deformation profiles when a distributed load was applied.

As shown in Figs. 4 and 5, the maximum deformation occurs in the simple plate. Nevertheless, since the designed sensor has to be integrated with a grasper and the teeth are required for better grasping capability, the simple plate is not a good option. Between the remaining two designs, the check configuration shows the larger deformation and, hence, the higher sensitivity. Therefore, the check teeth arrangement was chosen for microfabrication.

V. NUMERICAL RESULTS

In order to find a relationship between the output voltages of PVDF sensing elements and the applied load and to characterize the designed sensor, a number of loading scenarios was considered. This way, a series of calibration curves were obtained with which, using an inverse algorithm, it is possible to determine what grasping forces were actually applied during the application.
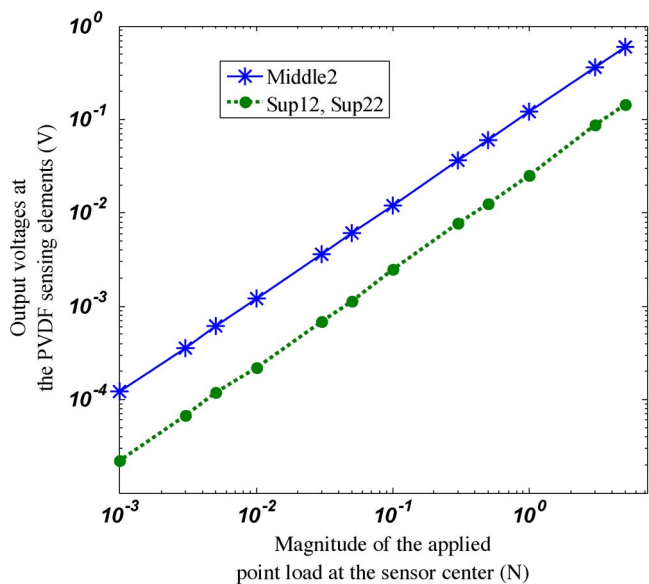
Fig. 6. Output voltages of PVDF sensing elements when point loads with different magnitudes were applied at the center of the sensor. Sup12 and Sup22 stand for Support12 and Support 22, respectively.

Fig. 7. Notations of the PVDF sensing elements. To generate this pattern, the aluminum coating on one side of a piece of piezoelectric PVDF film was patterned, as shown in this figure.

A. Force-Voltage Characteristic of PVDF Sensing Elements

In the first simulation, a point load was applied on the center of the silicon plate. The magnitudes of forces varied between two designed range limits—a maximum of 5 N for firm grasping and a minimum of 1 mN as a small mechanical force which could be comparable to artery pulses. At each load magnitude, output voltages at the PVDF sensing elements were recorded. Some of the calibration curves are shown in Fig. 6. The relative positions of active sensing elements are shown in Fig. 7.

As the calibration curves show, there is a linear relationship between the output voltage of each PVDF sensing element and the magnitude of applied load. The output voltages of the supports are identical because the load was applied at the center and thus carried equally by the two supports. It can also be seen that at each load magnitude, the output voltage of the middle PVDF layer is much higher than the output voltages of the PVDF at the supports. This is because the middle PVDF works in an extensional mode, whereas PVDF films at the supports work in a thickness mode. The PVDF layer at the middle is more sensitive and suitable for detecting the low-magnitude forces such as the pulse in blood vessels.

B. Force Position

In MIS, finding the position of a concentrated load is very important, as it could be used in determining the positions of a variety of hidden anatomical features. When a soft tissue without any embedded feature is grasped, the stress profile recorded at the surface is a kind of uniform (or at least smooth) distributed load. However, in general, any hidden anatomical feature, such as a lump or a hollow tubular feature—whether with pulsation (e.g., arteries or veins) or without pulsation (e.g., ureters)—appears as a disruption in this uniform pressure distribution [31], [32].

For instance, when there is no lump within the grasped tissue, a uniform background pressure distribution (P_o) would be registered at the contact surface of the grasped object and at the sensor surface. However, when there is an embedded lump in a bulk soft tissue, a sudden jump in the normal stress would be observed. The peak stress value occurs exactly at the position of the lump. Fig. 8(a) shows a finite element model of a lump embedded in a slab of soft material, and a compressive load, simulating the grasped boundary conditions, is applied from the top and bottom. In the following simulations, the materials were assumed to be isotropic. The properties of soft material were considered as $E_t = 20$ kPa and $\nu = 0.49$, whereas Young's modulus is 200 kPa and $\nu = 0.4$ for the lump. The normal stress profile at the sensor surface (here, the bottom surface) is shown in Fig. 8(b) and (c). In Fig. 8(c), the stress values read at the contact surface (P) were normalized by dividing P with the background pressure P_o (i.e., pressure values when there is no lump). Fig. 8(c) shows a prediction of more than a 40% force increase at the location of the lump on the contact surface. A simple model of this behavior can be thought of as a point load that is superimposed on a uniform distributed load, as shown in Fig. 8(d).

The 2-D finite element model of a nonpulsating tubular feature embedded in a bulk soft tissue is shown in Fig. 9. This model can be seen as a void inside the tissue. To avoid unnecessary complexity, the material property of the feature wall was considered to be similar to the surrounding tissue. As shown in Fig. 9(a)–(c), when there was a void inside the grasped object, a sudden decrease at the position of the void was observed.

In Fig. 9(c), the calculated stress values (P) at the contact surface was normalized by dividing P with the background pressure P_o. A sudden decrease of the stress on the contact surface of about 65% is predicted for this scenario at the void location. Again, in this case, as shown in Fig. 9(d), the problem of finding a hidden anatomical feature is turned into finding the location of a point load.

This is also valid for a pulsating artery or vein. These pulsating features are dynamic, although can be considered as a void between two consecutive beats and seen as a lump during pulsation. Fig. 10 shows the transient stress profile at the contact surface. In this model, the pulse was simulated by applying a sinusoidal pressure to the internal wall of the void. As the simulations show, when there is no pulsation (i.e., at $t = 0$ s), there is a reduction in the normal stress. However, during the pulsation, the amplitude of the load starts increasing
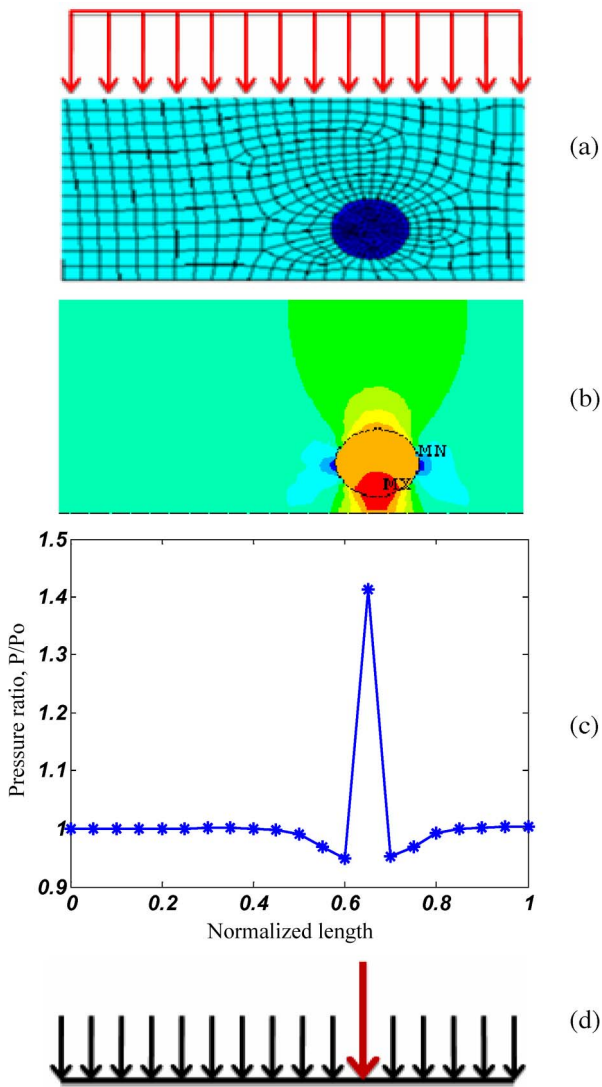
Fig. 8.   Finite-element model of the soft object with an embedded lump shows that the existence of a lump in a grasped soft object causes a sharp increase at the lump location to appear at the contact surface.

and reaches its maximum when the pulse is in its peak value (here, $t = 0.3$ s).

From these simulations, it was concluded that if a sensor system is capable of detecting and locating concentrated loads, it is potentially able to detect and locate a variety of hidden anatomical features, such as lumps or voids with pulsating/nonpulsating tubular features.

In order to evaluate the capability of the sensor to determine the point loads, a known point load was applied onto the silicon layer at different points of even intervals. Points of examination were chosen to be in the y-direction at the middle of the length and then to move in the x-direction at the middle of the width. Points of the load application are shown in Fig. 11. Output voltages of the PVDF sensing elements at supports are recorded and compared. The voltage curves versus locations of the point loads in the y-direction at different loading magnitudes are shown in Fig. 12.

The maximum voltage of the PVDF layer at support #1 occurs when the point load is applied on top of support #1
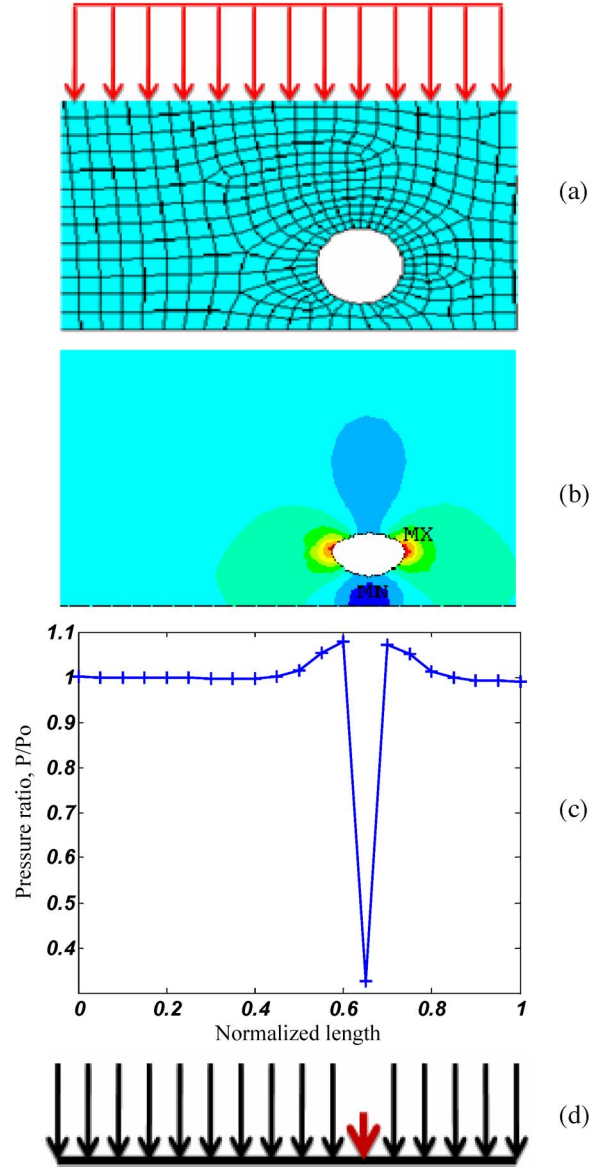

Fig. 9.   Finite-element model of the soft object with an embedded void shows that the existence of a void in a grasped soft object causes a sharp decrease at the void location to appear at the contact surface.
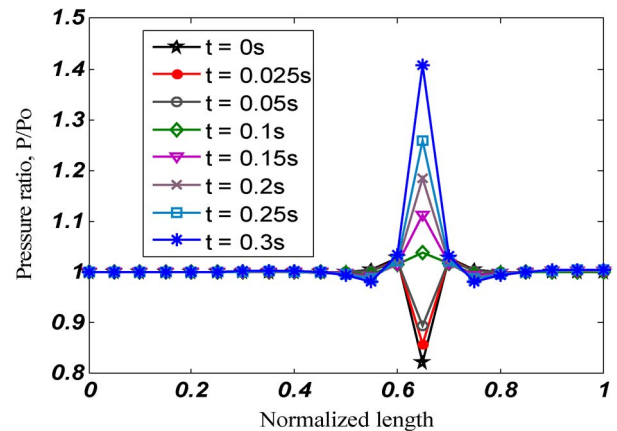

Fig. 10.   Normal stress distribution at the contact surface when a pulsating feature, embedded in the tissue, is calculated.
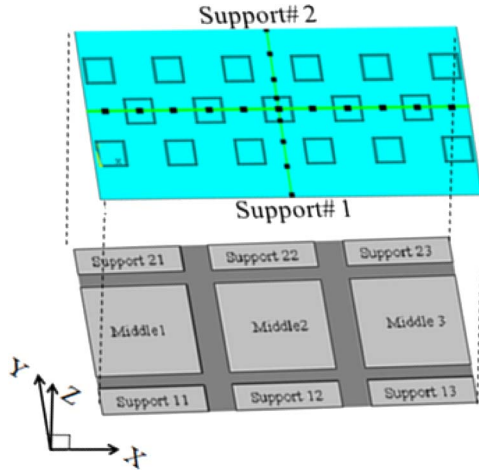
Fig. 11. Positions of the applied point load along the x- and y-directions are shown as black squared points on the silicon layer, and the corresponding sensing elements are shown underneath.
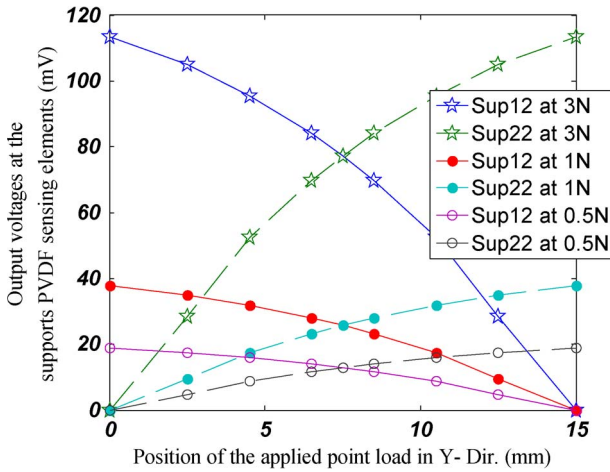

Fig. 12. Output voltage of PVDF sensing elements versus locations of the load in the y-direction. Sup12 and Sup22 are the shortened forms of Support12 and Support22, respectively.

$(y = 0)$. The voltage then decreases when the load location moves away until reaching minimum voltage when the load is applied at the top of support #2 ($y = 15$ mm). On the other side, the output voltage of the PVDF layer at support #2 starts from a minimum value when the load is applied on top of support #1 and then increases correspondingly when the load location moves further away until finally reaching the maximum output voltage when the load is applied on top of support #2. The output voltages on both PVDF layers at supports #1 and #2 equal each other when the load acts at the center point ($y = 7.5$ mm).

The output voltages of the sensing elements at the supports versus x location of the 1-N point load are shown in Fig. 13.

As shown in Fig. 13, the output voltages at Support11 and Support21 (the first support's pair) are always equal because the location of the applied load was always on the center between both and the compression load was divided equally. Moreover, the sensing elements Support12 and Support22 (the second support's pair) have the same output voltages for the same reason. This also applies to sensing elements Support13 and
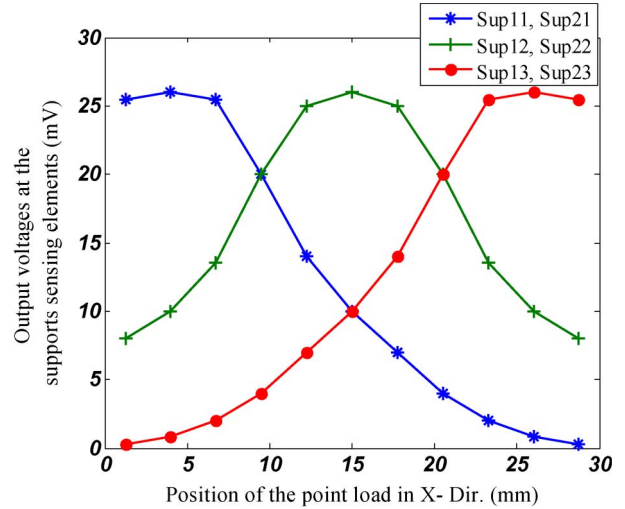

Fig. 13. Output voltages at the support PVDF sensing elements when a moving point load of 1-N magnitude is applied along the x-direction. Sup11, Sup21, Sup12, Sup22, Sup13, and Sup23 stand for Support11, Support21, Support12 Support22, Support13, and Support23, respectively.

Support23 (the third support's pair), where both have the same output voltages.

From Fig. 13, it is clearly shown that the output voltages at Support11 and Support21 on one side and at Support13 and Support23 on the other side are a mirror image of each other and are equal when $x = 15$ mm (center point of the plate). When $x = 4$ mm, voltages at Support11 and Support21 are maximum because the load is directly acting on the vertical line passing through their centers. The same rationale applies to Support13 and Support23 in which the output voltages are initially low and become higher, reaching a maximum when the load is acting on $x = 26$ mm. This is because the load is acting on the vertical line passing their centers directly. The load is directly on a vertical line passing through the centers of Support12 and Support22 when $x = 15$ mm and the output voltages on that sensing elements are maximum.

VI. SENSOR MICROFABRICATIONS AND ASSEMBLY

Three steps were required for sensor microfabrication. First, the silicon (top) plate had to be etched anisotropically. In parallel, the PVDF film had to be patterned. Finally, silicon plate and patterned PVDF were assembled on a Plexiglas support. The details of these steps are described in the following.

A. Silicon Micromachining

The upper layer of the proposed sensor was tetramethyl ammonium hydroxide (TMAH) etched from 500-μm-thick (100) silicon wafer, using MEMS technology. It is anisotropically etched to form the rigid toothlike structures; each tooth has a trapezoidal prism shape having an anisotropic etching angle of 54.74° on the sidewalls. The height of the prism tooth is equal to 200 μm; the depth of the etched U channel on the back is also 200 μm, and, finally, the remaining thickness of the etched layer is 100 μm. The steps of the microfabrications process are shown in Fig. 14.
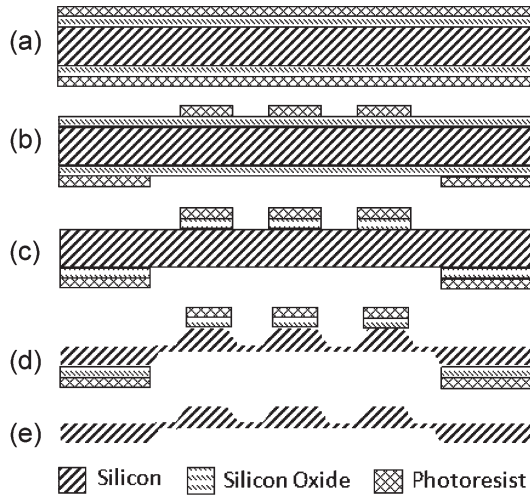
Fig. 14. Microfabrication process of the silicon layer. (a) Oxidizations and double-sided PR deposition. (b) UV exposure, hard baking, and PR developing. (c) Silicon oxide etching. (d) TMAH silicon etching. (e) Removal of the remaining PR and silicon oxide.
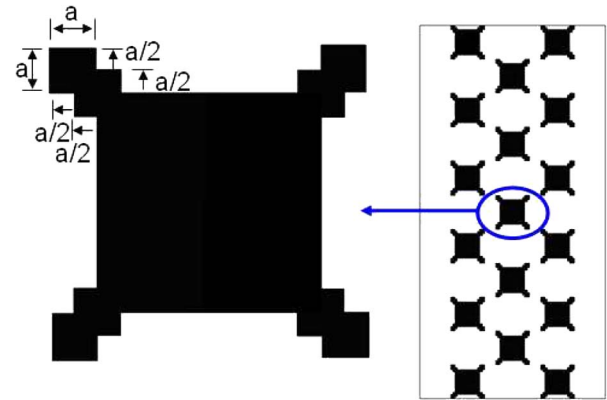

Fig. 15. Corner compensated light field mask applied to the polished face of the silicon sample.
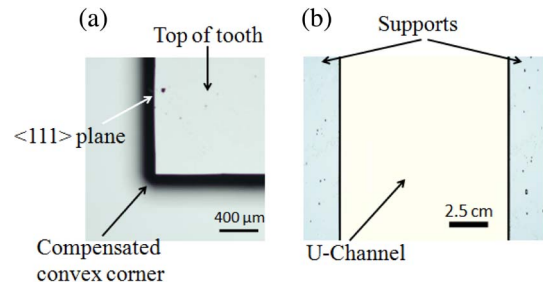

Fig. 16. Micromachined silicon layer. (a) Top view of the microfabricated silicon layer showing one compensated corner of tooth and the $\langle 111 \rangle$ side walls. (b) Back view showing the two supports and the U channel.

After wafer cleaning, the upper layer was wet oxidized at 1100 °C for 2 h to build up a silicon oxide layer of around 1.2-μm thickness on both sides.

A double-sided photolithography was used. First, the back surface of the silicon wafer was covered with a layer of S1813 positive photoresist (PR) by spin coating at 3000 r/min for a total time of approximately 45 s, which was followed by oven soft baking at 110 °C for 40 min, and then, the same steps were also repeated on the polished face, as shown in Fig. 14(a).

For this sensor design, two different light field masks were used; the first mask was used with the polished face of the sample to represent the teeth shapes of the sensor, and the second mask was used to represent the U channel and the supports on the back of the sample. The convex corners were protected and compensated using corner compensation techniques which were presented in some previous works [33]–[35]. For our design, the same method of compensations with KOH etching, which is presented in [33], was used to protect the convex corner with our TMAH bulk etching. The mask and the dimensions of the compensators used in this paper are shown in Fig. 15. The following equation was used to calculate the required dimensions of the squares [33]. $a = h/0.544$, where "h" is the etching depth and "a" is the side length of the squares. Since the desired depth was 200 μm, the compensator side "a" was found to be 367 μm. Using a mask aligner, both sides of the wafer were exposed to UV light for 15 s. The oven hard baking at 110 °C for 40 min was followed by a PR developing step [Fig. 14(b)].

The next step was the wet etching of the silicon oxide in buffered oxide etch to form a hard mask of silicon bulk etching [Fig. 14(c)]. The silicon was then etched inside a TMAH 25% bath at a temperature of 80 °C [Fig. 14(d)]. To guarantee a good etch rate, the samples were held vertically on a special holder while a magnet stirrer was rotating at the bottom of the beaker. The previous characterization tests showed that the etch rate of silicon in the $\langle 100 \rangle$ direction at the similar condition was around 24 μm/h [36]–[38]. Therefore, after 8.5 h of etching,

the etched depth was checked under the microscope, and the required 200-μm depth on each side was verified. Finally, the remaining PR and silicon oxide were removed, as shown in Fig. 14(e). Optical photographs of the microfabricated layer are shown in Fig. 16. The compensated convex corner and the $\langle 111 \rangle$ sidewalls of the tooth prism shape are shown in Fig. 16(a), and the U channel, as well as the two microfabricated supports on the back, is shown in Fig. 16(b).

B. PVDF Patterning

The metalized PVDF film, supplied by Good Fellow Co., has 3-GPa modulus of elasticity, 1.76-g/cm^3 density, and 0.35 Poisson's ratio. Its piezoelectric properties are 20 pC/N, 2 pC/N, −18 pC/N, 0.15 Vm/N, 0.015 Vm/N, and −0.15 Vm/N for d_{31}, d_{32}, d_{33}, g_{31}, g_{32}, and g_{33}, respectively [39].

At first, a PVDF film was cut into a 30×15 mm rectangle in such a way that the drawn direction (d_{31}) of the PVDF film aligned with the shorter dimension of the sample [i.e., y-direction; Fig. 17(a)]. Since one PVDF film was used for the middle and the two supports, one side of the sample PVDF film was patterned to be used as the positive electrode at the middle, as well as at the supports. The second side of the PVDF layer was kept without patterning to work as the common electrode for all sensing elements. Since the PVDF film was very thin and flexible, it was not possible to hold it on the suction chuck of the PR spinner. Therefore, a glass slide was used to support the PVDF sample while spinning. The glass support was also used in the baking, UV exposure, and patterning stages. The
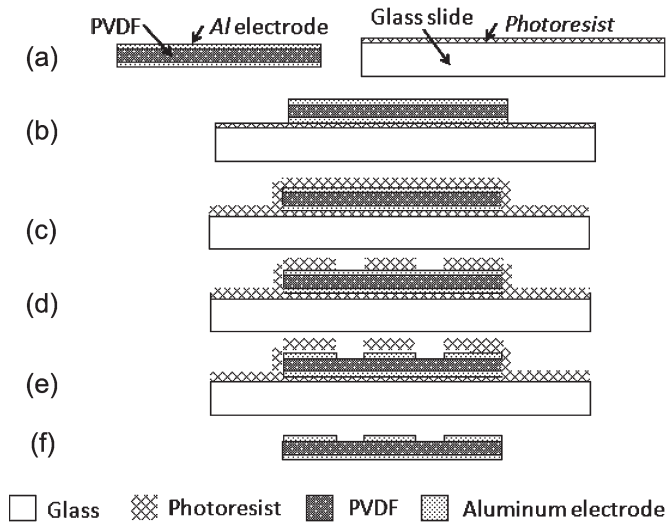
Fig. 17. PVDF film patterning process steps. (a) Preparing the metalized PVDF film, preparing and cleaning the glass slide, and depositing a PR on the glass slide to be used later as glue between the slide and the PVDF film. (b) Sticking the PVDF film to the glass slide. (c) PR deposition. (d) UV exposure, hard baking, and PR developing. (e) Aluminum electrode etching. (f) Removing the remaining PR and detaching the patterned PVDF film from the glass slide.
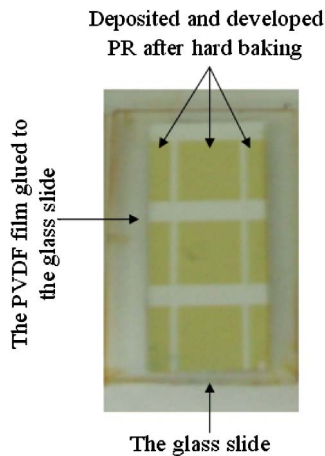

Fig. 18. PVDF sample after the hard-baking step.

PVDF sample was glued to the glass slide using PR. To do this, the glass slide was first PR spun coated [Fig. 17(a)], and then, the PVDF layer was carefully attached to its top [Fig. 17(b)]. The PR between the glass slide and the PVDF was also used to protect the aluminum coating of the backside. The PVDF was baked in the baking oven at 50 °C for a few minutes to make sure that the PVDF was glued to the PR properly. Then, the PVDF film was spun coated with S1813 positive PR [Fig. 17(c)]. To remove the undesirable metal coating, a mask for the sample was designed and aligned to the sample carefully, and then, the sample was exposed to UV light for 15 s. Then, the sample was developed by dipping it inside a beaker filled with PR developer for around 1–3 min [Fig. 17(d)]. The sample was stored inside a beaker filled with deionized water for a few minutes. This was followed by hard baking of the sample inside a baking oven at 50 °C for 40 min. In Fig. 18, the sample after the hard-baking stage is shown.
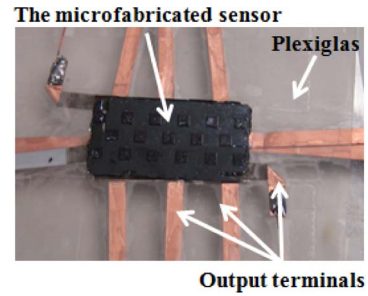

Fig. 19. Assembled sensor layers and the output terminal connections.

The aluminum coating was then etched for about 1 min in a beaker filled with commercial aluminum etchant type-A solution [40], which was heated at 50 °C using a hot plate [Fig. 17(e)]. Finally, the remaining PR is removed, and the PVDF film is detached from the glass slide [Fig. 17(f)].

As mentioned previously, the drawn direction (d_{31}) of the PVDF film was aligned with the shorter dimension of the sample (i.e., y-direction) for higher sensitivity of the sensor; however, in the ultimate product, the PVDF must be deposited. In the case of deposition, there would be no preferred directions (no uniaxial and no biaxial). Therefore, for the final product, the device must be characterized based on the deposition scenario.

C. Sensor Assembly

In the assembling step, a thin layer of nonconductive glue was applied uniformly to the etched U channel and the supports surfaces and kept for 5 min in the baking oven at 50 °C to spread out on the surfaces uniformly. Then, the PVDF layer was carefully aligned under a magnification lens and smoothly attached to the U channel and support surfaces. Out of ten wires, nine wires were connected to the nine PVDF sensing elements formed at the metalized areas using conductive epoxy glue. The common electrode on the backside of the PVDF film was connected to the tenth wire. The complete assembled sensor is shown in Fig. 19.

As it can be seen, this sensor is manually prototyped and assembled using glue. Securing PVDF in place using glue is challenging in terms of uniformity and diligence it requires and is only intended for prototyping. In the ultimate product of this prototype, as soon as the PVDF can be directly deposited on the microfabricated silicon layer, there is no need for gluing. Moreover, by the PVDF direct deposition, the advantages of the present design, including the low cost and ease of microfabrication and assembly, will be revealed.

VII. EXPERIMENTS

To characterize the sensor, a series of experiments were carried out. In order to obtain two sets of comparable data, the parameters in these experiments were the same as those used in the simulations.

A. Experimental Setup

A schematic diagram of the experimental measurement setup, developed to analyze the performance of the sensor, is
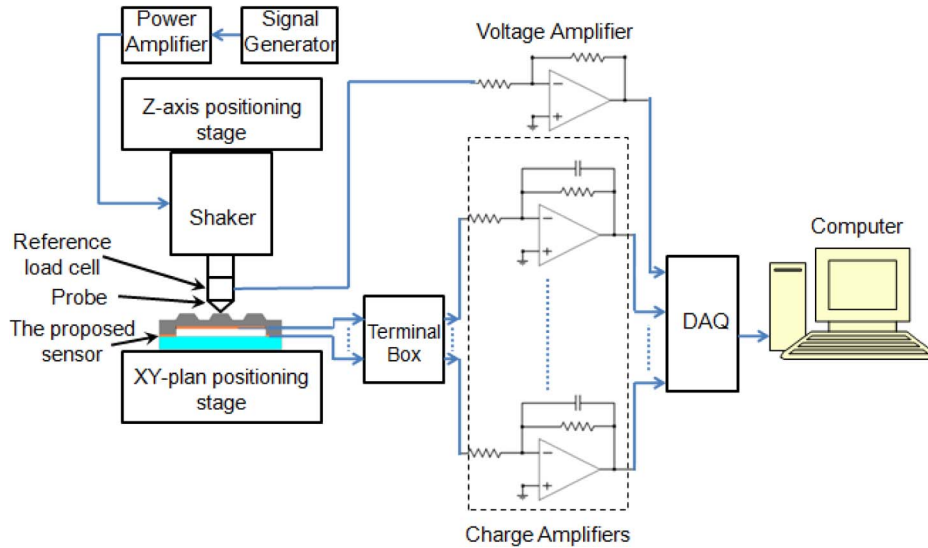
Fig. 20. Experimental setup used for the characterization of the proposed sensor.
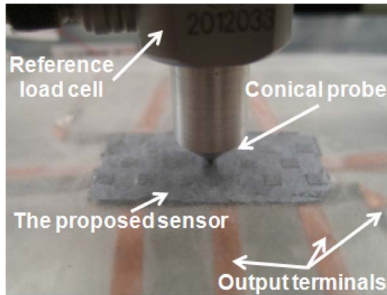

Fig. 21. Conical probe with a sharp tip for point load applications positioned on the sensor center.
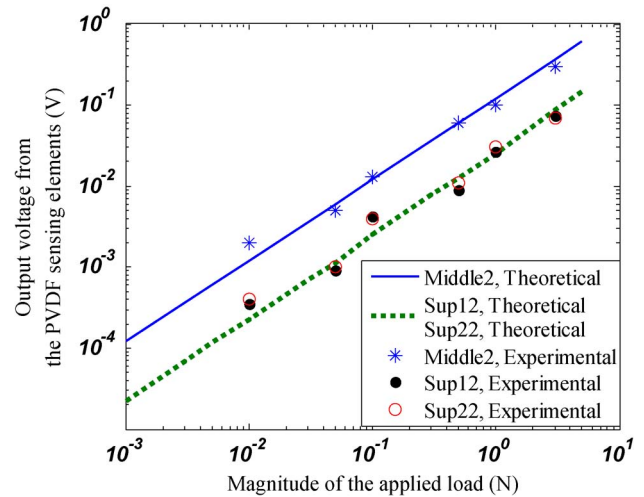

Fig. 22. Experimental data when a point load applied at the center of a sensor is compared with data from finite element modeling. Sup12 are Sup22 are the shortened forms of Support12 and Support22, respectively.

shown in Fig. 20. The sensor, as shown in Fig. 21, was positioned under a conical probe, which was driven by a vibration unit (Ling dynamic model V203) and used to apply a sinusoidal force. The frequency and amplitude of the vibration unit were controlled by a signal generator (Agilent 33220A). The magnitude of the applied force was determined by a reference load cell (KISTLER, Type 9712B50-Voltage mode), which was placed between the probe and the vibration unit. The load sensor was connected to a voltage amplifier for amplifications and then connected to a data-acquisition card (DAQ) to measure the actual applied load magnitude on the computer. Similarly, the PVDF sensing elements were connected through wires to the charge amplifiers, and then, the output of the charge amplifiers were connected to the DAQ to be measured on the computer. Therefore, signals were amplified and then digitized and filtered using DAQ. The 60-Hz line noise was filtered out using the Labview built-in Butterworth low-pass filter.

A complete cycle of closing and opening a MIS grasper is about 1 s. Therefore, the frequency of the grasping repetition is about 1 Hz. In addition, the acquired signal for one grasping action is very similar to a half sinusoidal waveform. Furthermore, the power spectrum of a grasping action shows that the power of frequencies more than 5 Hz is negligible [41]. Thus, the frequency of the sinusoidal force used in this section was chosen to be 5 Hz.

B. Experimental Results

Three sets of experiments were performed using the mentioned experimental setup. Through these experiments, the linearity of the sensor, with respect to the magnitude of the applied load, and the capability of the sensor to locate the force position in the x- and y-directions were examined. In the second and third experiments, a constant concentric load of 1 N was applied on the sensor surface at different points one at a time. Analogous to the finite element analysis, points of examination were first chosen in the y-direction at the middle of the length and then in the x-direction and at the middle of the width, as shown in Fig. 11.

1) Linearity: Analogous to the simulations, the experimental tests were carried out with different loading conditions to verify the sensor performance. Fig. 22 shows the experimental results for concentric loads, ranging from 10 mN to 3 N, which were applied at the center of the sensor. The comparison
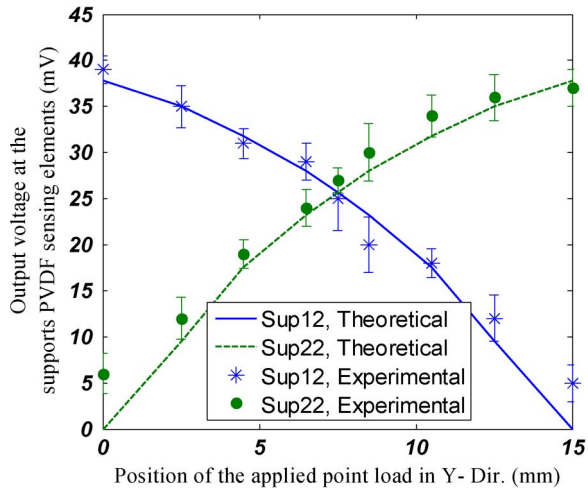
Fig. 23. Output voltages at the sensing elements when a moving concentric load is applied along the y-direction at equal intervals. Sup12 and Sup22 are the shortened forms of Support12 and Support22, respectively.
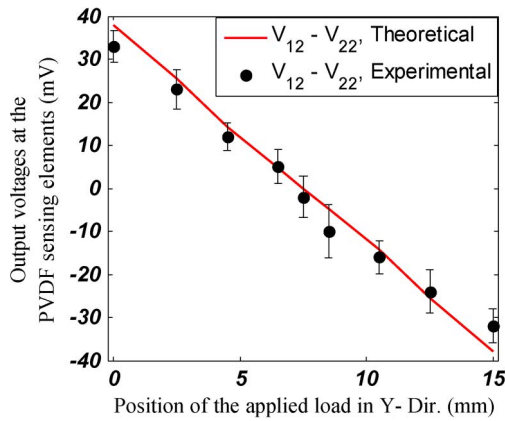

Fig. 24. When the point load moves along the sensor width, the difference between output voltages of the sensing elements Support12 (V_{12}) and Support22 (V_{22}) varies linearly.

between experimental results and simulations is also shown in Fig. 22.

2) Force Position, y-Direction: In these experiments the point load was applied to a series of points along the sensor width (in the y-direction) at even intervals. As shown in Fig. 23, the voltages of the two identical sensing elements of opposite supports (e.g., V_{12} for Support12 and V_{22} for Support22) were recorded. For the sake of comparison, the corresponding simulations are also plotted on the same graph. It is shown in Fig. 23 that when load is applied exactly onto the Support12 sensing element, this sensor generates the maximum potential while the sensing element at the opposite support shows no output. Accordingly, when the point of application moves away (along the y-direction), the output voltage of Support12 decreases, and that of Support22 increases. When load is applied exactly in the middle of the supports (i.e., $d = 7.5$ mm), the output voltage of the sensing element at both supports are equal. The same trend is seen when the location of the load passes the midpoint. It is interesting to know that the difference between the output voltages of each pair of sensing elements at the supports ($V_{12}-V_{22}$) is linear with respect to the location of the applied concentric load. This is shown in Fig. 24. Therefore,
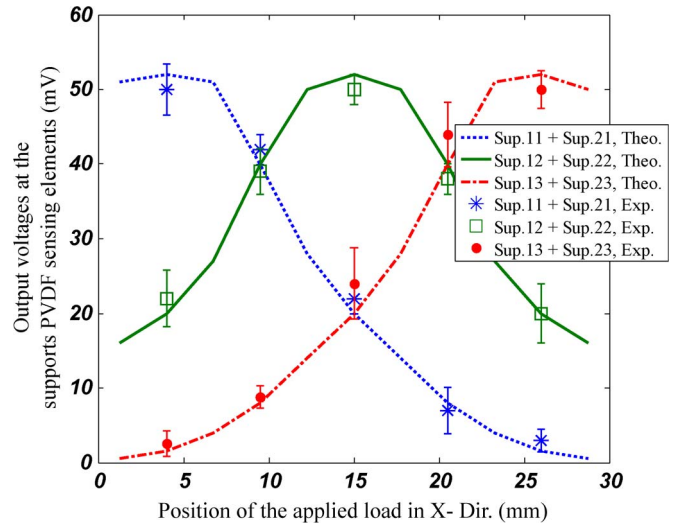

Fig. 25. Output voltages at the support sensing elements versus location of the moving point load in the x-direction. Sup11, Sup21, Sup12, Sup22, Sup13, and Sup23 stand for Support11, Support21, Support12 Support22, Support13, and Support23, respectively.
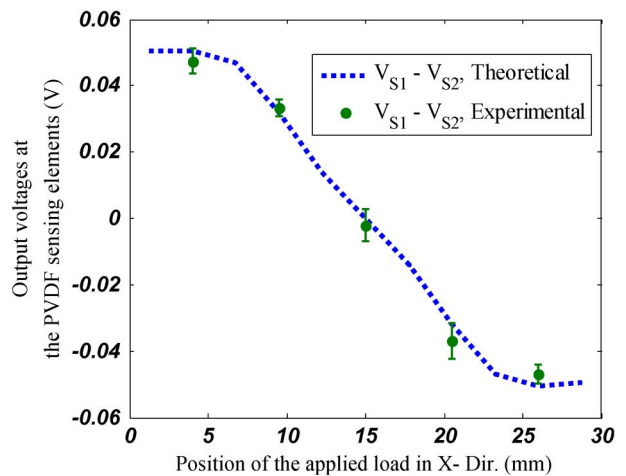

Fig. 26. Difference between V_{S1}, the summation of the output voltages of Support11 and Support21, and V_{S1}, the summation of the output voltages of Support13 and Support23, versus locations of the load in the x-direction is shown.

the location of the applied load in the y-direction can be computed, using this linear relation.

3) Force Position, x-Direction: An alternative experiment was performed in which the location of the point load was varied along the x-axis. Algebraic summations of the output voltages of each pair of sensing element at supports versus the x location of the applied load are shown in Fig. 25, in which the experimental and theoretical results are compared. The location of the applied point load on the x-direction can be calculated precisely using the curves of sensing element voltages versus the load location. For this purpose, the summation of the output voltages of Support11 (V_{11}) and Support21 (V_{21}) is calculated and referred to as V_{S1}. Alternatively, the summation of the output voltages of Support13 (V_{13}) and Support23 (V_{23}) is computed and called V_{S2}. As shown in Fig. 26, by comparing V_{S1} and V_{S2}, the location of the applied concentric load in the x-direction can be measured.

VIII. SUMMARY AND CONCLUSION

The importance of developing force sensors for use in MIS, which are capable of measuring applied load and its location, was discussed. These sensors are designed to be integrated within conventional MIS graspers. This category of smart endoscopic graspers is particularly useful for detecting hidden anatomical features, such as embedded lumps or arteries/veins, when tissue is grasped. When a uniform soft object is grasped, a uniform (or smooth) stress distribution at the surface of the tissue and sensor appears. However, the existence of any lumps superimposes a point load to the existing uniform load, adding a sharp increase at the place of the application. Alternatively, any hollow feature causes a sudden decrease in the background uniform stress distribution at the location of the feature. In both cases, the location of sudden change indicates the position of the hidden feature. It was also shown that a pulsating artery, although a dynamic input, can be modeled as a time-varying concentrated load lying on a plane normal to the artery.

In this paper, a sensor capable of measuring the magnitude of a point load, as well as its position on the surface of the sensor, was designed, microfabricated, and characterized. The corrugated shape of the sensor helps for better grasping of any slippery tissues. The sensing flexible surface was made out of a (100) silicon wafer. For this paper, the support was selected to be Plexiglas, although it can also be manufactured using silicon wafer or polymers. The piezoelectric PVDF film was used as the transduction material as it exhibits good performance in both extensional and thickness mode. After micromachining the silicon part and pattering the PVDF film, the sensor was assembled. The entire surface of the sensor is active, which can be considered as one of the distinguishing advantages of this sensor in comparison with other tactile sensors introduced for MIS. In addition, the device was designed in such a way that does not require oriented PVDF and is, therefore, amenable to fabrication using deposition. The simplicity of the sensor for microfabrications is another important feature.

A series of experiments was conducted on the sensor, and corresponding simulations were carried out, using a finite element model. A good match between numerical results and experiments were observed. Although the ability of the sensor to detect a lump or other embedded features was not experimentally verified, simulations have confirmed that this sensor is potentially capable of detecting and locating a wide range of hidden features in the grasped object. This tactile sensor was primarily designed for endoscopic surgery; however, it can be used in conjugation with any delicate telemanipulation or robotic end effector, in which the accurate measurement of applied load and its position is important.

In this paper, the feasibility of using conventional MEMS technology in developing a novel PVDF-based sensor for use in MIS surgery was shown. In order to achieve further miniaturization, a monolithic approach would be needed. This method would require the PVDF solution to be deposited directly on the specified area, a step that could be accomplished using a variety of processes, including spin coating.

REFERENCES

[1] F. Tendick, S. S. Sastry, R. S. Fearing, and M. Cohn, "Applications of micromechatronics in minimally invasive surgery," *IEEE/ASME Trans. Mechatron.*, vol. 3, no. 1, pp. 34–42, Mar. 1998.

[2] R. Howe and Y. Matsuoka, "Robotics for surgery," *Annu. Rev. Biomed. Eng.*, vol. 1, pp. 211–240, 1999.

[3] M. Carrozza, P. Dario, and L. Jay, "Micromechatronics in surgery," *Trans. Inst. Meas. Control*, vol. 25, no. 4, pp. 309–327, Oct. 2003.

[4] M. A. Qasaimeh, I. Stiharu, and J. Dargahi, "Design and analysis of a micromachined tactile sensor for minimally invasive surgery," in *Proc. Int. Conf. Dyn., Instrum. Control*, Queretaro, Mexico, Aug. 13–16, 2006.

[5] G. Tholey, A. Pillarisetti, W. Green, and J. Desai, "Design, development, and testing of an automated laparoscopic grasper with 3-D force measurement capability," in *Proc. ISMS,* S. Cotin and D. Metaxas, Eds., 2004, vol. 3078, pp. 38–48.

[6] M. A. Qasaimeh, J. Dargahi, M. Kahrizi, and M. Packirisamy, "Design and analysis of tactile optical sensor for endovascular surgery," in *Proc. Photon. North Conf.*, Ottawa, ON, Canada, Jun. 4–7, 2007.

[7] R. Howe, W. Peine, D. Kontarinis, and J. Son, "Remote palpation technology," *IEEE Eng. Med. Biol. Mag.*, vol. 14, no. 3, pp. 318–323, May/Jun. 1995.

[8] K. Rebello, "Applications of MEMS in surgery," *Proc. IEEE*, vol. 92, no. 1, pp. 43–55, Jan. 2004.

[9] M. Ottermo, O. Stavdahl, and T. Johansen, "Palpation instrument for augmented minimally invasive surgery," in *Proc. IEEE/RSJ Int. Conf. Intell. Robots Syst.*, Sendai, Japan, Sep. 28, 2004, pp. 3960–3964.

[10] W. Peine, J. Son, and R. Howe, "A palpation system for artery localization in laparoscopic surgery," in *Proc. 1st Int. Symp. Med. Robot. Comput.-Assisted Surg.*, Pittsburgh, PA, Sep. 22–24, 1994, pp. 250–253.

[11] F. Nahas, A. Farah, and D. Solia, "Suspicious node found at the time of reduction mammaplasty," *Aesthet. Plast. Surg.*, vol. 26, no. 1, pp. 54–56, Jan. 2002.

[12] Y. Kuroda, M. Nakao, T. Kuroda, H. Oyama, and M. Komori, "Interaction model between elastic objects for haptic feedback considering collisions of soft tissue," *Comput. Methods Programs Biomed.*, vol. 80, no. 3, pp. 216–224, Dec. 2005.

[13] A. Melzer, G. Buess, and A. Cuschieri, "Instruments and allied technology for endoscopic surgery," in *Operative Manual of Endoscopic Surgery 2*. New York: Springer-Verlag, 1994, pp. 1–69.

[14] J. G. Webster, *Tactile Sensors for Robotics and Medicine*. New York: Wiley-Interscience, 1988.

[15] A. Golpaygani, S. Najarian, and G. Emamieh, "Design and modeling of a new tactile sensor based on membrane deflection," *Amer. J. Appl. Sci.*, vol. 4, no. 10, pp. 813–819, 2007.

[16] R. Chen and B. Wang, "The use of polyvinylidene fluoride films as sensors for the experimental modal analysis of structures," *Smart Mater. Struct.*, vol. 13, no. 4, pp. 791–799, Aug. 2004.

[17] J. Dargahi, M. Parameswaran, and S. M. Payandeh, "A micromachined piezoelectric tactile sensor for an endoscopic grasper—Theory, fabrication and experiments," *J. Microelectromech. Syst.*, vol. 9, no. 3, pp. 329–335, Sep. 2000.

[18] N. Narayanan, A. Bonakdar, J. Dargahi, M. Packirisamy, and R. Bhat, "Design and analysis of a micromachined piezoelectric sensor for measuring the viscoelastic properties of tissues in minimally invasive surgery," *Smart Mater. Struct.*, vol. 15, no. 6, pp. 1684–1690, Dec. 2006.

[19] J. Dargahi, S. Najarian, R. Ramezanifard, and F. Ghomshe, "Fabrication and testing of a medical surgical instrument capable of detecting simulated embedded lumps," *Amer. J. Appl. Sci.*, vol. 4, no. 5, pp. 957–964, 2007.

[20] S. Sokhanvar, M. Packirisamy, and J. Dargahi, "A multifunctional PVDF-based tactile sensor for minimally invasive surgery," *Smart Mater. Struct.*, vol. 16, no. 4, pp. 989–998, Aug. 2007.

[21] M. Metha, "A micromachined capacitive pressure sensor for use in endoscopic surgery," M.S. thesis, School Eng. Sci., Simon Fraser Univ., Burnaby, BC, Canada, 1996.

[22] K. Suzuki, K. Najafi, and K. D. Wise, "A 1024-element high-performance silicon tactile imager," *IEEE Trans. Electron Devices*, vol. 37, no. 8, pp. 1852–1860, Aug. 1990.

[23] Samaun, K. D. Wise, and J. B. Angell, "An IC piezoresistive pressure sensor for biomedical instrumentation," *IEEE Trans. Biomed. Eng.*, vol. BME-20, no. 2, pp. 101–109, Mar. 1973.

[24] Y. S. Lee and K. D. Wise, "A batch-fabricated silicon capacitive pressure transducer with low temperature sensitivity," *IEEE Trans. Electron Devices*, vol. ED-29, no. 1, pp. 42–48, Jan. 1982.

[25] H. Tanigawa, T. Ishihara, M. Hirata, and K. Suzuki, "MOS integrated silicon pressure sensor," *IEEE Trans. Electron Devices*, vol. ED-32, no. 7, pp. 1191–1195, Jul. 1985.

[26] A. Menciassi, A. Eisinberg, M. Carrozza, and P. Dario, "Force sensing microinstrument for measuring tissue properties and pulse in microsurgery," *IEEE/ASME Trans. Mechatron.*, vol. 8, no. 1, pp. 10–17, Mar. 2003.

[27] C. Sauer, D. Tomlin, H. Naeini, O. Gerovichev, and N. Thakor, "Real-time measurement of blood vessel occlusion during microsurgery," *Comput. Aided Surg.*, vol. 7, no. 6, pp. 364–370, 2002.

[28] S. Sokhanvar, M. Ramezanifard, J. Dargahi, and M. Packirisamy, "Graphical rendering of localized lumps for MIS applications," *Trans. ASME, J. Med. Devices*, vol. 1, pp. 217–224, 2007.

[29] ANSYS Inc., *ANSYS Release 8.0 Documentation*, Jan. 2007.

[30] ANSYS Inc., *Coupled- Field Analysis Guide, ANSYS Release 10.0*, 2005.

[31] S. Hosseini, S. Najarian, S. Motaghinasab, A. Golpaygani, and S. Torabi, "Prediction of tumor existence in the virtual soft tissue by using tactile tumor detector," *Amer. J. Appl. Sci.*, vol. 5, no. 5, pp. 483–489, 2008.

[32] M. Hosseini, S. Najarian, S. Motaghinasab, and J. Dargahi, "Detection of tumours using a computational tactile sensing approach," *Int. J. Med. Robot. Comput. Assisted Surg.*, vol. 2, no. 4, pp. 333–340, Dec. 2006.

[33] W. Fan and D. Zhang, "A simple approach to convex corner compensation in anisotropic KOH etching on a (1 0 0) silicon wafer," *J. Micromech. Microeng.*, vol. 16, no. 10, pp. 1951–1957, Oct. 2006.

[34] H. Schröder, E. Obermeier, A. Horn, and G. Wachutka, "Convex corner undercutting of {100} silicon in anisotropic KOH etching: The new step-flow model of 3-D structuring and first simulation results," *J. Microelectromech. Syst.*, vol. 10, no. 1, pp. 88–97, Mar. 2001.

[35] H.-Y. Chu and W. Fang, "A novel convex corner compensation for wet anisotropic etching on (100) silicon wafer," in *Proc. 17th Micro Electro Mech. Syst. Conf.*, Maastricht, The Netherlands, Jan. 25–29, 2004, pp. 253–256.

[36] W. Sonphao and S. Chaisirikul, "Silicon anisotropic etching of TMAH solution," in *Proc. IEEE Int. Symp. Ind. Electron.*, 2001, pp. 2049–2052.

[37] I. Stateikina, L. M. Landsberger, M. Kahrizi, N. Hoque, and V. Rossokhaty, "Silicon wet etch anisotropy: Analysis of the impact of {111}-, {110}-, {100}-terrace widths," *Sens. Mater.*, vol. 17, no. 4, pp. 201–213, 2005.

[38] L. Landsberger, S. Naseh, M. Kahrizi, and M. Paranjape, "On hillocks generated during anisotropic etching of Si in TMAH," *J. Microelectromech. Syst.*, vol. 5, no. 2, pp. 106–116, Jun. 1996.

[39] Good Fellow Corporation, Data retrieved on March 2007. [Online]. Available: http://www.goodfellow.com/csp/active/gfHome.csp

[40] K. R. Williams, K. Gupta, and M. Wasilik, "Etch rates for micromachining processing—Part II," *J. Microelectromech. Syst.*, vol. 12, no. 6, pp. 761–778, Dec. 2003.

[41] S. Sokhanvar, M. Ramezanifard, J. Dargahi, M. Packirisamy, and W. Xie, "The force and softness signature in minimally invasive surgery graspers," in *Proc. CSME/SCGM*, Ottawa, ON, Canada, Jun. 5–8, 2008.

Saeed Sokhanvar received the B.Sc. degree in mechanical engineering from the University of Tehran, Tehran, Iran, the M.Sc. degree in biomechanical engineering from Sharif University of Technology, Tehran, in 1994, and the Ph.D. degree in mechanical engineering from Concordia University, Montreal, QC, Canada, in 2007.

He was with the medical device industry for nine years. Since 2007, he has been with the BioInstrumentation Laboratory, Massachusetts Institute of Technology, Cambridge, as a Postdoctoral Fellow. His research interests include biomechanics and bioinstrumentation, specifically modeling of physiological systems, soft tissue mechanics, minimally invasive surgery, haptic/tactile devices, and diagnostic and drug delivery devices.

Javad Dargahi received the B.Sc. and M.Sc. degrees in mechanical engineering from the University of Paisley, Paisley, U.K., and the Ph.D. degree in the area of robotic tactile sensors from Glasgow Caledonian University, Glasgow, U.K., in 1993.

He was an Assistant Professor in the Biomedical Engineering Department, Amirkabir University of Technology, Tehran, Iran, in 1994. He was a Senior Postdoctoral Research Associate (Visiting Professor) with the Micromachining/Medical Robotics Group, Simon Fraser University, Burnaby, BC, Canada, in 1997. He was a full-time Lecturer in the Mechanical Engineering Department, University of New Brunswick, Fredericton, NB, Canada, in 1999. He was with Pega Medical Company, Montreal, QC, Canada, in 2001. He joined Concordia University, Montreal, as an Assistant Professor in September 2001. He received his tenure and was promoted to Associate Professor in June 2006 and is currently with the Tactile Sensing and Medical Robotics Laboratory, Department of Mechanical and Industrial Engineering. His research interests include design and fabrication of haptic sensors and feedback systems for minimally invasive surgery and robotics, micromachined sensors and actuators, and teletaction. He is the author of 60 journal and 60 refereed conference papers. He is a coauthor of the book *Artificial Tactile Sensing in Biomedical Engineering* (to be published by McGraw-Hill in January 2009).

Mohammad Ameen Qasaimeh received the B.Sc. degree in mechanical/mechatronics engineering from Jordan University of Science and Technology, Jordan, in 2005, and the M.A.Sc. degree in mechanical engineering from Concordia University, Montreal, QC, Canada, in 2007. He is currently working toward the Ph.D. degree in the Micro and Nanobioengineering Laboratory, Biomedical Engineering Department, Faculty of Medicine, McGill University, Montreal.

He is concerned with the field of microelectromechanical systems (MEMS) and tactile sensation in minimally invasive surgery applications. His current research interests include BioMEMS, microfluidic probes and devices, neuronal navigation devices, lab-on-a-chip devices, single-cell electroporation and biochemical gradient chips, implanted microelectrodes for brain activity measurement, and microtactile devices for minimally invasive surgery.

Mojtaba Kahrizi (M'02) received the Ph.D. degree in applied solid-state physics from Concordia University, Montreal, QC, Canada, in 1985.

After spending five years at St. Francis Xavier University, Antigonish, NS, Canada, as a Research Associate and Assistant Professor, in 1991, he came back to Concordia University, joining the MEMS and Nanodevice Laboratories, Department of Electrical and Computer Engineering. He established the Micro Devices and Microfabrication Laboratories in that department. He has been involved with teaching and research in the areas of material sciences, solid-state devices, MEMS, photonics, and nanoscience and nanotechnology. He is the author or a coauthor of more than 150 journal and conference papers.

Dr. Kahrizi a member of the Professional Engineers of Ontario. He is also a member of the Center for Applied Research on Polymers and Composite and the Center for Biorecognition and Biosensors. He is the Chair of the IEEE Electron Devices Society Montreal chapter.